Magnetotellurics and Airborne Electromagnetics as a combined method for assessing basin structure and geometry.

Thesis submitted in accordance with the requirements of the University of Adelaide for an Honours Degree in Geophysics.

Millicent Crowe

October 2012

THE UNIVERSITY of ADELAIDE

MAGNETOTELLURICS AND AIRBORNE ELECTROMAGNETICS AS A COMBINED METHOD FOR ASSESSING BASIN STRUCTURE AND GEOMETRY.

MT & AEM AS A COMBINED EXPLORATION METHOD

ABSTRACT

Unconformity-type uranium deposits are characterised by high-grade and constitute over a third of the world's uranium resources. The Cariewerloo Basin, South Australia, is a region of high prospectivity for unconformity-related uranium as it contains many similarities to an Athabasca-style unconformity deposit. These include features such as Mesoproterozoic red-bed sediments, Paleoproterozoic reduced crystalline basement enriched in uranium (~15-20 ppm) and reactivated basement faults. An airborne electromagnetic (AEM) survey was flown in 2010 using the Fugro TEMPEST system to delineate the unconformity surface at the base of the Pandurra Formation. However highly conductive regolith attenuated the signal in the northern and eastern regions, requiring application of deeper geophysical methods. In 2012 a magnetotelluric (MT) survey was conducted along a 110 km transect of the north-south trending AEM line. The MT data was collected at 29 stations and successfully imaged the depth to basement, furthermore providing evidence for deeper fluid pathways. The AEM data were integrated into the regularisation mesh as a-priori information generating an AEM constrained resistivty model and also correcting for static shift. The AEM constrained resistivity model best resolved resistive structures, allowing strong contrast with conductive zones. There was not enough resolution in the MT models to establish the presence of uranium mineralisation.

KEYWORDS

Magnetotellurics, electromagnetic induction, airborne electromagnetics, static shift,

Cariewerloo Basin, Pandurra Formation, uranium, exploration, unconformity

TABLE OF CONTENTS

LIST OF FIGURES AND TABLES

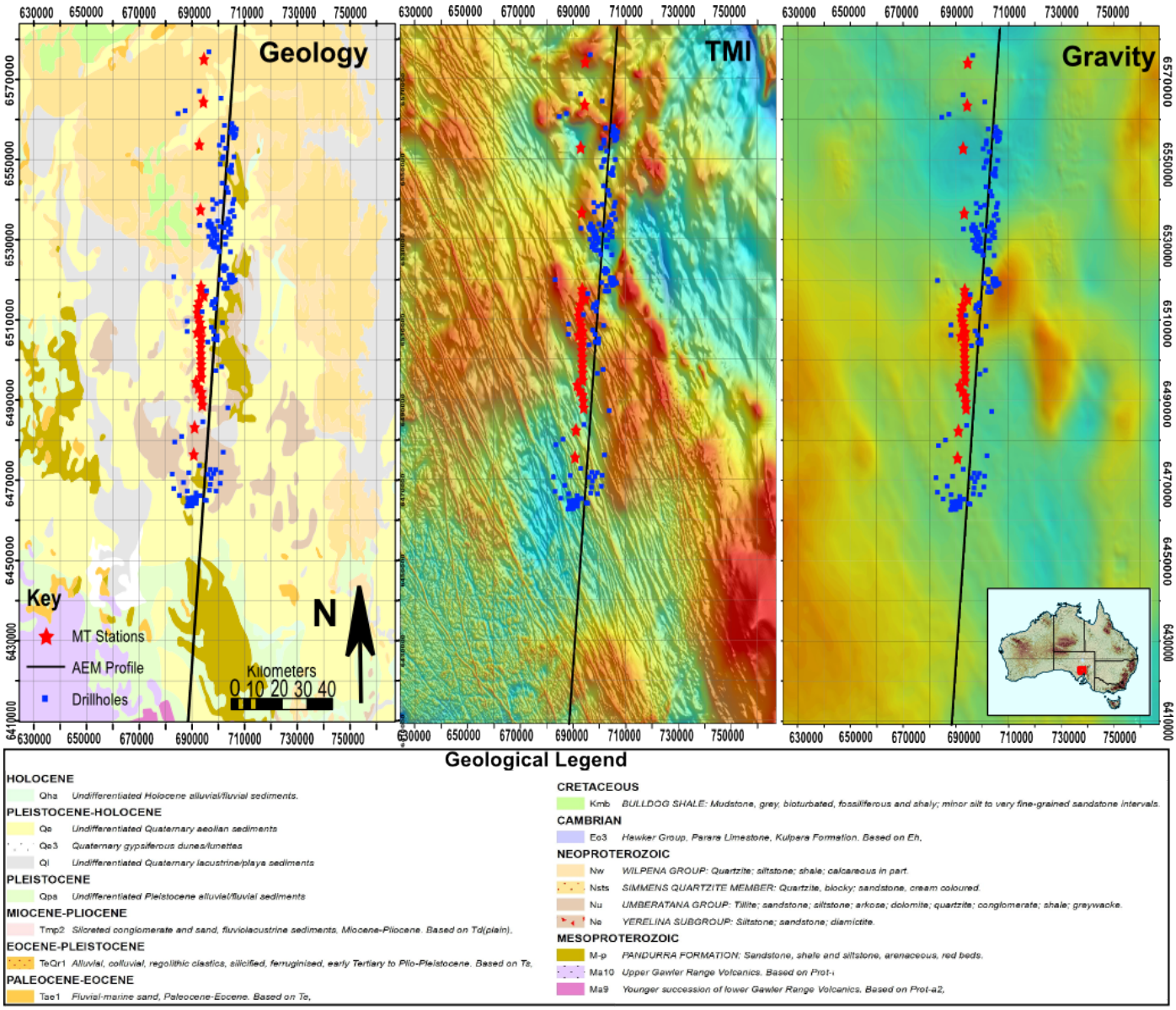

Figure 1 Geological, gravity and magnetic (TMI) maps of the Cariewerloo Basin, South Australia, overlain with AEM survey line 700201 (black line), 29 MT stations (red stars), drill holes within a 13km radius of the AEM line (blue dots). The MT survey line consists of 29 broadband MT stations recording at 1000 Hz for two days. Inset: Map of Australia showing the map extent in red.

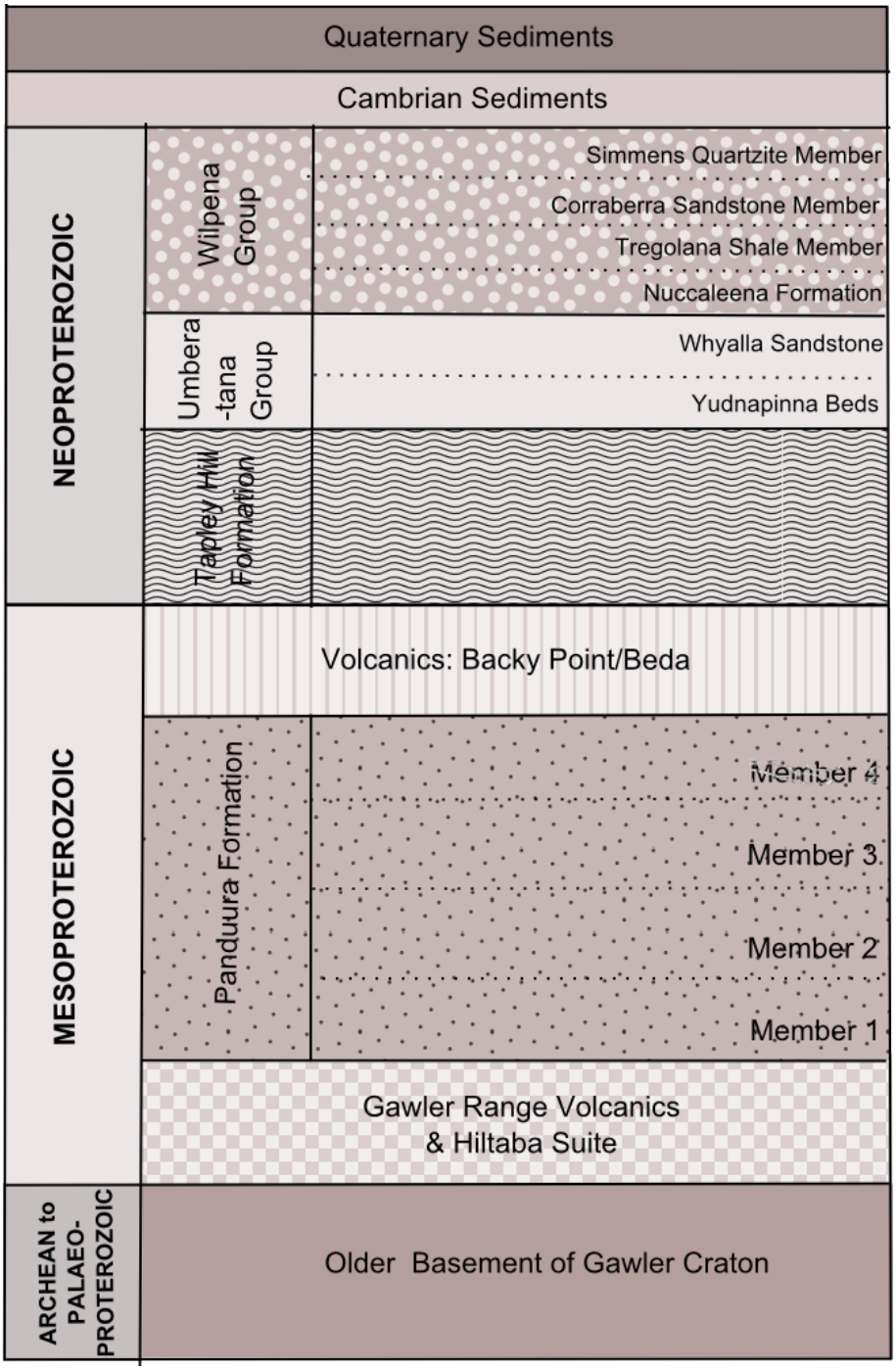

Figure 2 Stratigraphic column of the Cariewerloo Basin adapted from Cowley (1991). Archaean to Paleoproterozoic Gawler Craton is overlain by uranium enriched Gawler Range Volcanics and the intrusive equivalent Hiltaba Suite granites, which is unconformably overlain by the Pandurra Formation, a medium-coarse grained sandstone. This is overlain by Adelaidean Sequences including the Tapley Hill Formation, Whyalla Sandstone, and other Quaternary sediments.

INTRODUCTION

Magnetotellurics (MT) can be an effective tool for investigating basement geology in regions with significant amounts of conductive cover. The Cariewerloo Basin, South Australia, is such an area where highly conductive regolith is present to extensive depths (>500 m). It has been a region of interest since 2000 as it displays criteria considered essential for unconformity-related uranium mineralisation, such as uranium enriched Hiltaba Suite granites, oxidised redbed sandstone, and reactivated basement faults (Fairclough 2006). In 2010 an Airborne Electromagnetic (AEM) Survey, using the Fugro TEMPEST System, was flown in the southern margins of the basin that successfully mapped the shallow basement (<300 m) (Dhu *et al.* 2010a). However, significant amounts of conductive cover attenuated the signal, leaving deeper basement depth to the northeast unknown (Dhu *et al.* 2010b). Mineralisation is thought to occur at, above or below the unconformity. By mapping the depth to basement, and consequently the unconformity surface, it is expected that possible locations for uranium mineralisation can be identified from conductive anomalies in the resistive sandstone. This study aims to map the depth to basement and consequently the unconformity surface, demonstrating MT and AEM are more useful together as a combined method than either method individually.

The Cariewerloo Basin exhibits characteristics similar to that of the Athabasca Basin, Canada and is thought to have the potential to host unconformity-related uranium mineralisation zones (Wilson *et al.* 2010a). Tuncer *et al.* (2006) conducted a high frequency MT study on the Athabasca Basin, concluding MT imaged conductive anomalies known to be graphitic structures and alteration halos associated with the

mineralisation to a depth of 2-3 km (Tuncer *et al.* 2006), which demonstrates the applicability of MT in exploration for this style of uranium deposit.

In this study, 29 broadband MT stations were deployed along a 110 km segment of a previously flown north-south AEM line (Figure 1). It is expected that an AEM constrained MT model will better define the depth to basement in areas of > 300 m cover and provide evidence for deeper flow paths in the basement. Additionally the AEM data will also be used to evaluate the effect of static shift on the MT data.

UNCONFORMITY-HOSTED URANIUM DEPOSITS

There are many styles of uranium deposit, with only four types actively explored for in South Australia. These include breccia complexes, sandstone (roll front) style mineralisation, vein-related mineralisation and unconformity-related mineralisation (Fairclough 2006). The highest grade uranium resources are unconformity-related and constitute ~33% of the western world's uranium resources (de Veslud *et al.* 2009, Cameco Corporation 2010, World Nuclear Association 2010). The largest high-grade unconformity-related uranium mines are found in the Athabasca Basin, Canada (Wilson *et al.* 2010b) with McArthur River uranium deposit reserve estimated at 778 500 t ore at 19.53% of U_3O_8 and Cigar Lake uranium deposit estimated at 557 300 t at 17.04% U_3O_8 (Cameco Corporation 2010). Other unconformity-related deposits include the Alligator

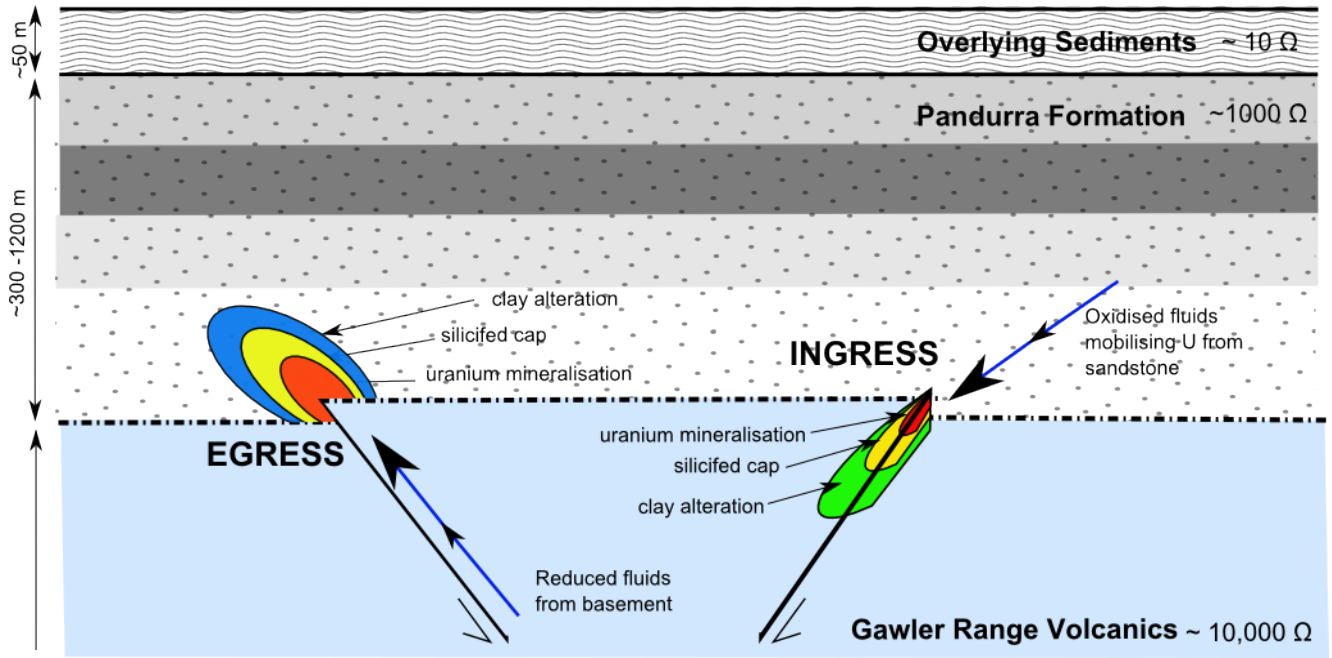

Figure 3 Schematic diagram of an unconformity related uranium deposit adapted from Tuncer *et al.* (2006). There are two types of unconformity deposits; egress (right) and ingress (left). Egress-type deposits are formed when reduced basement fluids flow into the sandstone reacting with oxidised fluids. Ingress-type deposits are formed when oxidised basinal fluids flown along faults into the basement, reacting with reduced basement lithologies. Ingress-type deposits are smaller than Egress-type, but both generally show mineralisation surrounded by a silicified cap with clay alteration.

River region in the Northern Territory, which hosts 19% of Australia's known uranium resources (Lambert *et al.* 2005).

In unconformity-related uranium deposits, zones of mineralisation are found below, at or immediately above the unconformity (Wilson *et al.* 2010b). There are currently two theories on the origin of uranium in these deposits; the first suggests the uranium is mobilised by oxidising basinal fluids from the sandstone which precipitates upon contact with reducing rock types or basement fluids (Wilson & Kyser 1987, Fayek & Kyser 1997) known as ingress-type deposits (figure 2). They are fracture controlled and found in dipping shear zones containing disseminated and massive uraninite and pitchblende (Jefferson *et al.* 2007). An alternate model suggests that fluids leach uranium from basement rocks and precipitated by the redox change at the unconformity (Hecht & Cuney 2000, Derome *et al.* 2003). Egress deposits are found at or above the unconformity surface (within ~25 m), have an elongate, cigar shape and often show clay bounded mineralisation as a high-grade core with a low-grade alteration halo. The Alligator Rivers type deposits are hosted below the unconformity in the basement, whereas the Cigar Lake and McArthur River are situated in the sandstones that immediately overlie the unconformity (Alexandre *et al.* 2009).

Circulating basement fluids have the potential to mobilise the anomalously high levels of uranium present in the Gawler Range Volcanics and Hiltaba Suite (Cowley 1993). The faults and unconformity surfaces provide potential fluid pathways, enabling the oxidised fluids to migrate due to gravity and/or tectonic processes (Skirrow 2009). These fluids may then interact with beds of reduced lithologies found in the Pandurra

Formation, precipitating any mineralisation (Keeling *et al.* 2011). Likewise, evidence from Fanning *et al.* (1983) stated the Pandurra Formation is derived from the Gawler Range Volcanics, so is also likely to be enriched in uranium, providing potential for enriched basinal fluids to precipitate ingress type deposits. Thus the Cariewerloo Basin is prospective for the potential to host both ingress and egress type uranium deposits.

The Pandurra Formation has undergone two significant events; diagenesis and influx of fluids. Evidence exists for diagenesis with detrital feldspars and muscovite forming crystalline kaolinite, dickite and the regional alteration signature of a haematitic – kaolinite matrix (Fanning *et al.* 1983). Where potassium has been reintroduced, dickite tends towards hairy illite. Evidence for fluid migration within the Pandurra Formation exists where the oxidised red sandstone is locally bleached or appears green in sections, adjacent with to typical fluid pathways such as fractures, faults and contacts (Cowley 1991). Mineralogical evidence for fluid migration is seen in the presence of phengite and dickite (Keeling *et al.* 2011). Identification of these minerals provides a target for electromagnetic exploration due to their high conductivity against the resistive sandstone.

GEOLOGICAL SETTING

The Cariewerloo Basin is a Mesoproterozoic intracontinental sedimentary basin that unconformably overlies the eastern margin of the Gawler Craton (Figure 3) (Cowley 1991). The Gawler Craton is a late Archaean-Mesoproterozoic crystalline basement that was assembled to its current form *ca*. 2000-1450 Ma in association with the Sleaford and Kimban Orogenies (Hand *et al.* 2007). The Mesoproterozoic Gawler

Range Volcanics are the magmatic equivalent of the Hiltaba Suite Granites, both of which have a close association with the formation of Iron Oxide Copper Gold ± Uranium (IOCG±U) deposits found at Olympic Dam and Prominent Hill (Belperio & Freeman 2004).

The Cariewerloo Basin is an elongated north-west trending sedimentary basin that is 120 km wide extending for 500 km. It is bounded by northwest trending faults with basement highs at Mt Gunson and Olympic Dam (Cowley 1993), which are displaced by younger northeast trending faults. Within the Cariewerloo Basin, the Pandurra Formation is the unit of interest. It is made up of a thick succession of Mesoproterozoic, unmetamorphosed and undeformed fluvial redbed sediments. The Pandurra Formation is overlain by Adelaidean sequences including the Tapley Hill Formation, a grey carbonaceous shale intercalated with carbonate; Whyalla sandstone, a coarse redbed sandstone with a fissile red shale member and Quaternary Sediments which thicken toward north (Cowley 1993). A stratigraphic column further describing the geology of the Cariewerloo Basin can be observed in Figure 2.

The Pandurra Formation varies in thickness from 300 m to 1200 m and is relatively flat lying, dipping approximately 15˚ to the north-east. Deposition is thought to precede faulting due to the relatively consistent internal stratigraphy. Siltstone dating on the Pandurra Formation indicates deposition occurred at 1424 ±51 Ma largely derived from the uranium enriched Gawler Range Volcanics (Fanning *et al.* 1983). Mason *et al.* (1978) and Tonkin (1980) informally divide the Pandurra Formation into four members

Member 1 – The basal unit with poorly sorted fine-medium grained lithic sandstone with interbeds of shale and siltstone with detrital chlorite. Bleached spots are common and indicative of fluid migration. The thickness of this member varies from 0-273 m, averaging 35-90 m (Cowley 1991).

Member 2 – The marker unit, a widespread micaceous sandy mudstone to siltstone with interbeds of sandstone. Thickness ranges from 3 - 109 m with an average of 10 – 65 m (Cowley 1991).

Member 3 – Fine to medium grained well-sorted sandstone with interbedded shale and micaeous siltstone, characteristic heavy mineral layering and cross bedding, gypsum nodules are locally present, mottled white with green and yellow spots and bands. Thickness ranges from 0 - 351 m averaging 100 - 200 m (Cowley 1991).

Member 4 – A cross-bedded medium grained to granular sandstone. There are thin interbeds of pebble conglomerate, mudstone, siltstone and fine-grained sandstone with heavy mineral banding and mottled bleaching. The top of this member is mostly eroded but ranges in thickness from 0–637 m, averaging 100–300 m (Cowley 1991).

The geological setting and age of the Cariewerloo Basin is very similar to that found in the Athabasca Basin, Canada, which hosts the largest unconformity-related uranium deposits in the world (de Veslud *et al.* 2009, Cameco Corporation 2010, World Nuclear Association 2010). Similarities include; Palaeo-Mesoproterozoic unmetamorphosed sedimentary rocks which unconformably overlie deformed and metamorphosed Palaeoproterozoic and Archaean basement, reactivated basement faults and elevated uranium concentration in basement rocks (Cowley 1991, Jefferson *et al.* 2007). There is interest in the potential for the Cariewerloo Basin to host an Athabasca-style uranium

deposit because it hosts many of the criteria considered essential for the unconformity-related uranium deposit model.

MAGNETOTELLURIC THEORY

MT is a passive EM technique that can image deep Earth structures and one aspect of the physical state of the crust and upper mantle (Simpson & Bahr 2005, Chave & Jones 2012). MT simultaneously records naturally occurring time dependent magnetic field fluctuations and the associated induced orthogonal electric current at the surface of the Earth (Tikhonov 1950, Cagniard 1953). The signal relies upon external quasi-uniform natural sources (Egbert 2002) recording between a frequency range of 10^4 Hz - 10^{-4} Hz. Frequencies greater than 1 Hz are induced from electric storms in the atmosphere; less than 1 Hz the source originates from the plasma waves in the ionosphere and magnetosphere (Viljanen *et al.* 2001).

The magnetic field is related to the electric field through the following equation;

$$\begin{bmatrix} E_x \\ E_y \end{bmatrix} = \begin{bmatrix} Z_{xx} & Z_{xy} \\ Z_{yx} & Z_{yy} \end{bmatrix} \begin{bmatrix} H_x \\ H_y \end{bmatrix} \qquad (1)$$

Where **E** is the electric field, **H** is the magnetic field and **Z** is the transfer function between the two horizontal fields, nominated the impedance tensor. The Fourier transform used to estimate the impedance tensor is estimated in the frequency domain. A linear least square (LS) method is used to find the best estimation of **Z** for each frequency. The impedance tensor elements provide information about the subsurface resistivity structure (Bedrosian 2007).

The skin depth equation is an important equation that describes how the electric field changes with depth in a homogenous half space earth.

$$D = \sqrt{\frac{2\rho}{\mu\omega}} \approx 500\sqrt{\frac{\rho}{f}} \qquad (2)$$

Where D is the skin depth (m), the depth at which 67 % of the signal is attenuated, ρ is the apparent resistivity (Ω.m), μ is the magnetic permeability (assumed to equal free space value μ_0) and ω is the angular frequency equal to 2πf, where f is frequency (Hz).

Equation 2 can be used to show that it is the frequency that sets the depth of investigation in EM techniques, with low frequencies penetrating to greater depths than high frequencies. However, the depth of investigation also depends on sampling rate, recording time, signal strength, site density and profile length.

MT provides information on the physical properties of the subsurface (specifically the conductivity) rather than defining the lithology directly, however, there is a strong correlation found between the two. MT is sensitive to electrically conductive phases in rock, such as fluid, melt, ore, graphite, sulphide or high temperature. Highly conductive features shield underlying structures, decreasing the resolution. This is known as the screening effect (Orange 1989, Bedrosian 2007, Thiel & Heinson 2010).

MT is susceptible to near surface distortion caused by conductive or resistive heterogeneous anisotropic layers (Berdichevsky & Logunovich 2008). Of particular importance is the static shift phenomenon where the apparent resistivity-sounding curve is shifted but the impedance phase is left unaffected (Jones 1988, Pellerin & Hohmann

1990). Static shift is caused by the electric field generated from boundary charges on inhomogeneities in the surface, causing erroneous data values due to the potential difference between electrode pairs not truly representing the horizontal electrical field component (Jones 1988). Time Domain Electromagnetics (TEM) is not affected by static shift, and is often used to correct for static shift by shifting apparent resistivity sounding curves to the values indicated by the TEM (Sternberg *et al.* 1985, Jones 1988, Sternberg *et al.* 1988, Pellerin & Hohmann 1990, Meju 1996, Macnae *et al.* 1998, Tournerie *et al.* 2007).

EM detects conductive anomalies which can be associated with key features of the unconformity-related model such as basal graphite bearing metapelite and faults (Ray et al 1976; Matthews et al. 1997). MT has been used in the Athabasca Basin for exploration for unconformity related uranium deposits (Tuncer *et al.* 2006). Subtle conductive anomalies are detectable against the resistive background of the sandstone in the Athabasca Group. These anomalies are due to conductive clay alteration halos associated with unconformity-related uranium deposits. Likewise quartz dissolution is strongly linked with egress type deposits and causes a conductive area which correlates to regions of structural disturbance and dissolution found within zones of uraninite. AMT detects deep conductors such as highly altered clay rich sandstone, which stand out against the silicified highly resistive sandstone. By using MT in the Cariewerloo Basin, similar conductive structures are expected to be identified if comparable alteration associated with uranium mineralisation is present.

METHODS

Data Acquisition

A two dimensional (2D) MT survey was acquired over a 10 day period in June 2012. There were 29 stations deployed with the majority of stations spaced 1 km apart and 6 outlying stations at 10 km spacing, along a 110 km transect at the northern end of the AEM line 7000201. Eight Auscope broadband MT instruments were used to collect the data. Each station recorded the geomagnetic North and East components of the electric and magnetic fields for two days, at a sample rate of 1000 Hz.

Magnetic field data were acquired using two induction coils placed orthogonal to each other in a geomagnetic north-south and east-west arrangement. The electric field data were captured using three non-polarising Cu-$CuSO_4$ electrodes with an average dipole length of 50 m in an L-shape configuration, which was aligned to geomagnetic North and East using a compass.

Data Processing

Coherent time series windows were selected and processed using a robust remote referencing code (Chave & Thomson 2004). This is a simple but effective tool to minimise bias due to local EM noise. The output response contained the impendance tensor for 46 frequencies over a bandwidth of 200 to 0.002 Hz, from which apparent resistivity and phase curves can be calculated. A notch filter was applied to remove noise observed at 50 Hz and subsequent harmonics.

DATA ANALYSIS

Strike Analysis

The electric current direction can be resolved with 90˚ ambiguity by analysing the geoelectric strike of each frequency. Shorter periods were random and showed no clear alignment of geoelectric strike angle, typical of a 1D environment where there is no clear polarisation of subsurface electric currents. Longer periods indicate the geoelectric strike converged at either 45˚ or 135˚ consistent with the Gawler Craton. The geological strike of the Cariewerloo Basin is 135˚, leading to the interpretation that the geoelectric strike of this data set is 135˚.

PT Pseudosection

It is important to understand the dimensionality of the data set to determine if 2D analysis is valid. In dimensionality analysis, the phase tensor is used with more confidence than the apparent resistivity as it is not affected by near surface distortion (Jones 1988). Phase tensor pseudosections are an elliptical representation of the phase tensor for each period in each stations, with shape of the ellipse indicating the dimensionality; circular ellipses are indicative of resistive regions of 1D while an elongated ellipse indicates a 2D or 3D region of resistivity which requires further analysis of the skew and ellipticity. For the purpose of this study, data points with skew angles $-5^\circ < \beta < 5^\circ$ and ellipticity larger than 0.1 are considered to be 2D.

A phase tensor pseudosection for the Cariewerloo MT Dataset is shown in Figure 4. At short periods (those less than 0.128 s) most phase tensor ellipses tend to be circular

indicating that the near surface resistivity is relatively 1D. At longer periods (0.853-20.5 s), the ellipses are more elongate suggesting that conditions become more 2D and possibly 3D at depth. Further analysis of the longer periods show the skew is generally ~3˚ and ellipticity less than 0.1 indicating mostly 2D effects with some minor 3D effects at very long periods. These findings for long period are consistent with the strike at the edge of the eastern Gawler Craton, representing the contact between resistive Archaean core and the more conductive Proterozoic fold belts (Heinson et al. 2006). For the majority of the bandwidth, the data are consistent with shallow 1D structure with some 2D effects caused by basin sediments and basement topography, indicating 2D analysis is valid.

Apparent Resistivity and Phase Curves

Typical apparent resistivity and phase curves calculated from the impedance tensor are shown in Figure 6. The TE mode is where electric current flows parallel to geoelectric strike (135˚) while the TM mode is perpendicular to electric current flow (45˚). Figure 6 illustrates the data are of good quality, continuous, consistent and relatively free from noise with 50 Hz peaks being corrected for using notch filters.

Phase and Apparent Resistivity Pseudosections

In a 2D Earth, the TE and TM modes are sensitive to different aspects of the subsurface structure, each showing different apparent resistivity values. The TE mode is most susceptible to along-strike conductors, whereas the TM mode is more sensitive to along strike resistors and perpendicular structures (Berdichevsky et al. 1998). Pseudosections are a convenient and easy way to compare the TE and TM modes. The pseudosection

illustrated in Figure 5 shows the TE mode, and to a greater extent the TM mode, are both sensitive to two vertical regions of higher resistive values than the surrounding area. Both the TE and TM modes show a linear conductive layer overlying a more resistive layer, with the TM observing more variation in the structure.

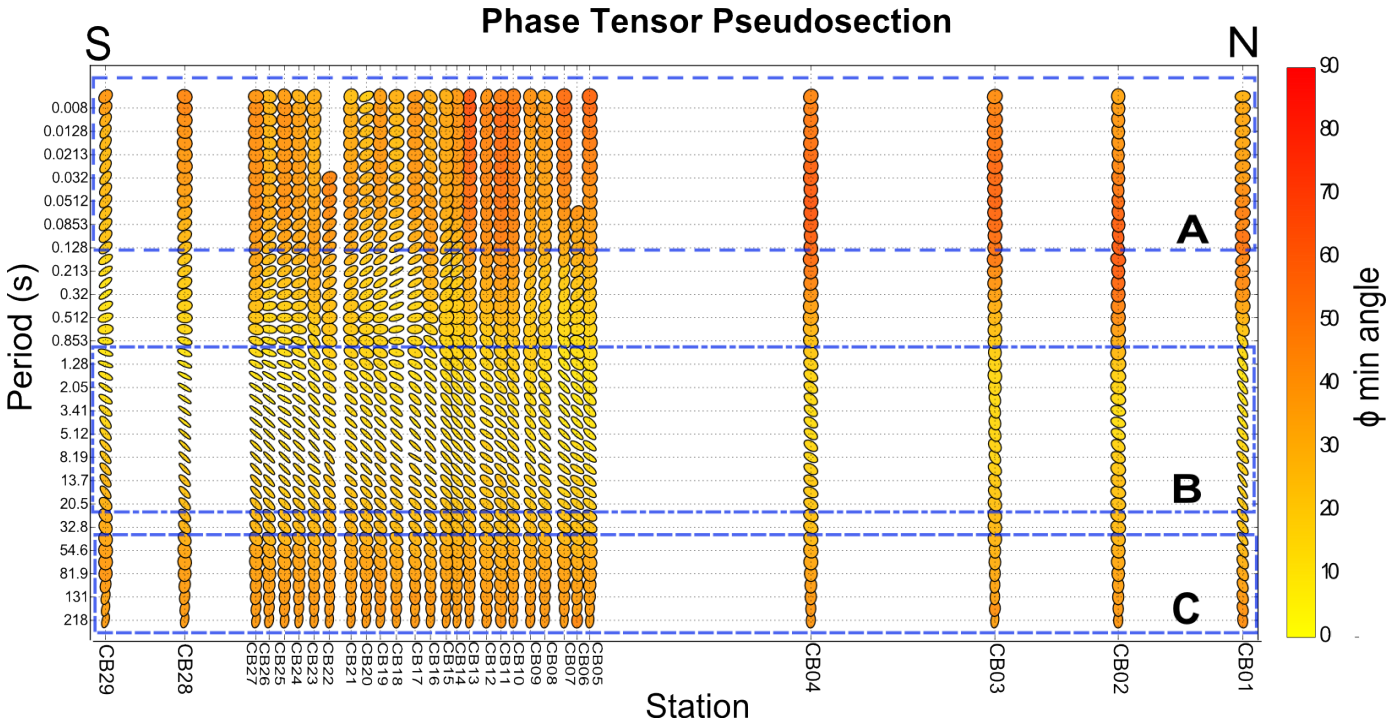

Figure 4 Phase Tensor Pseudosection of the Cariewerloo Basin, South Australia. The phase tensor is not susceptible to galvanic distortion so provides a robust estimation of the dimensionality. The shape of the ellipse indicates the dimensionality, the direction of elongation point in the direction of current flow with a 90° ambiguity. The phase tensor pseudosection of the Cariewerloo Basin can be divided into three broad regions; A is a region of short periods (shallow depths) which generally have circular ellipses with very little skew indicating this region is mostly 1D; B is a region showing elongated ellipses, pointing in a northwest – southeast direction indicating 2D or 3D body; C shows a region of circular and moderately circular ellipses, indicating the deepest region is predominately 2D or 3D region.

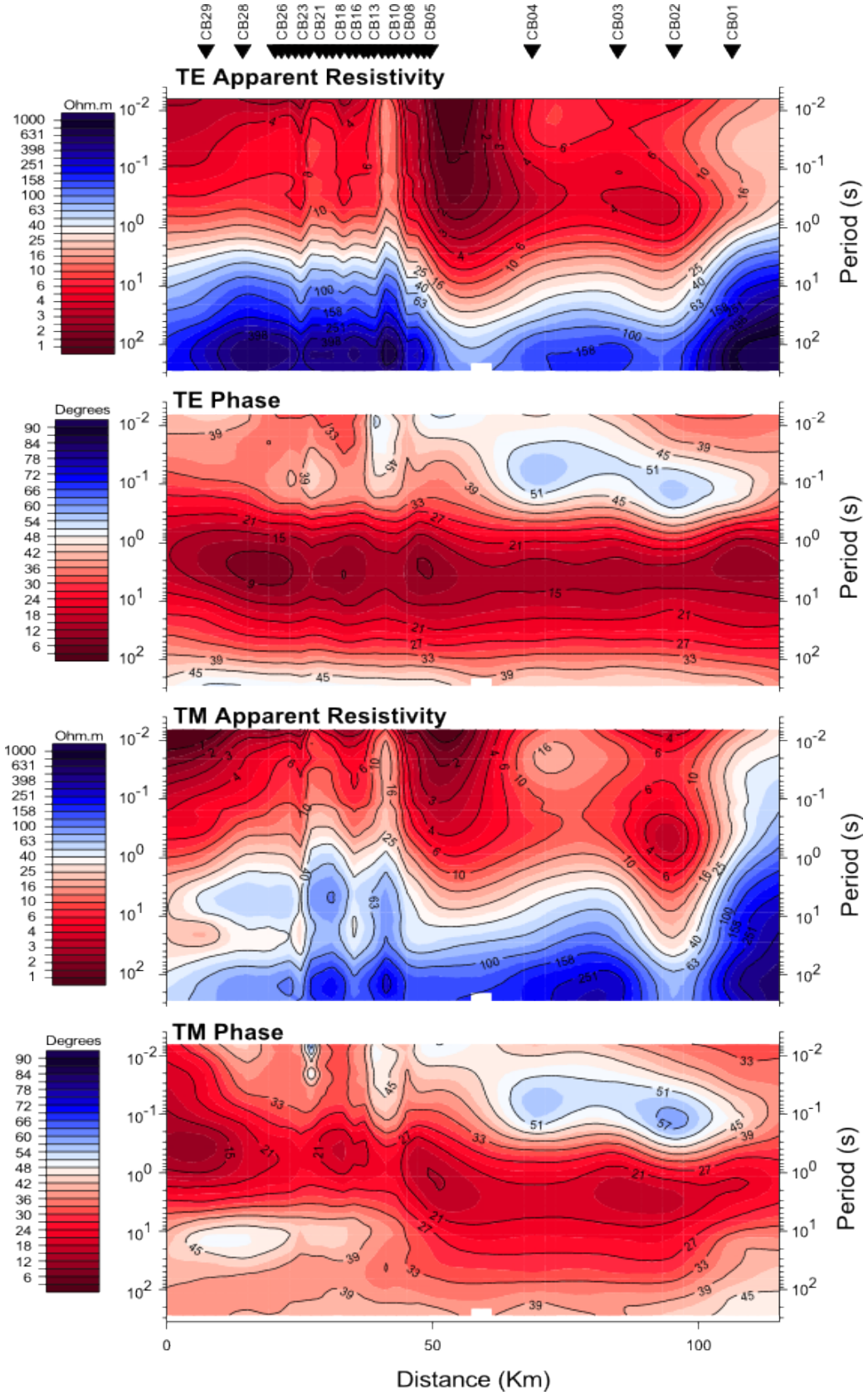

Figure 5 Apparent Resistivity and Phase Pseudosection of the MT data for the Cariewerloo Basin with a defined strike direction of 135°N. TE mode is most sensitive to along strike conductors where as TM a mode is most sensitive to along strike resistors. The general trend shows conductive region at shallow periods which becomes more resistive at longer periods. Two vertical anomalies can be observed under stations under CB10 and CB21 which are inferred to be faults.

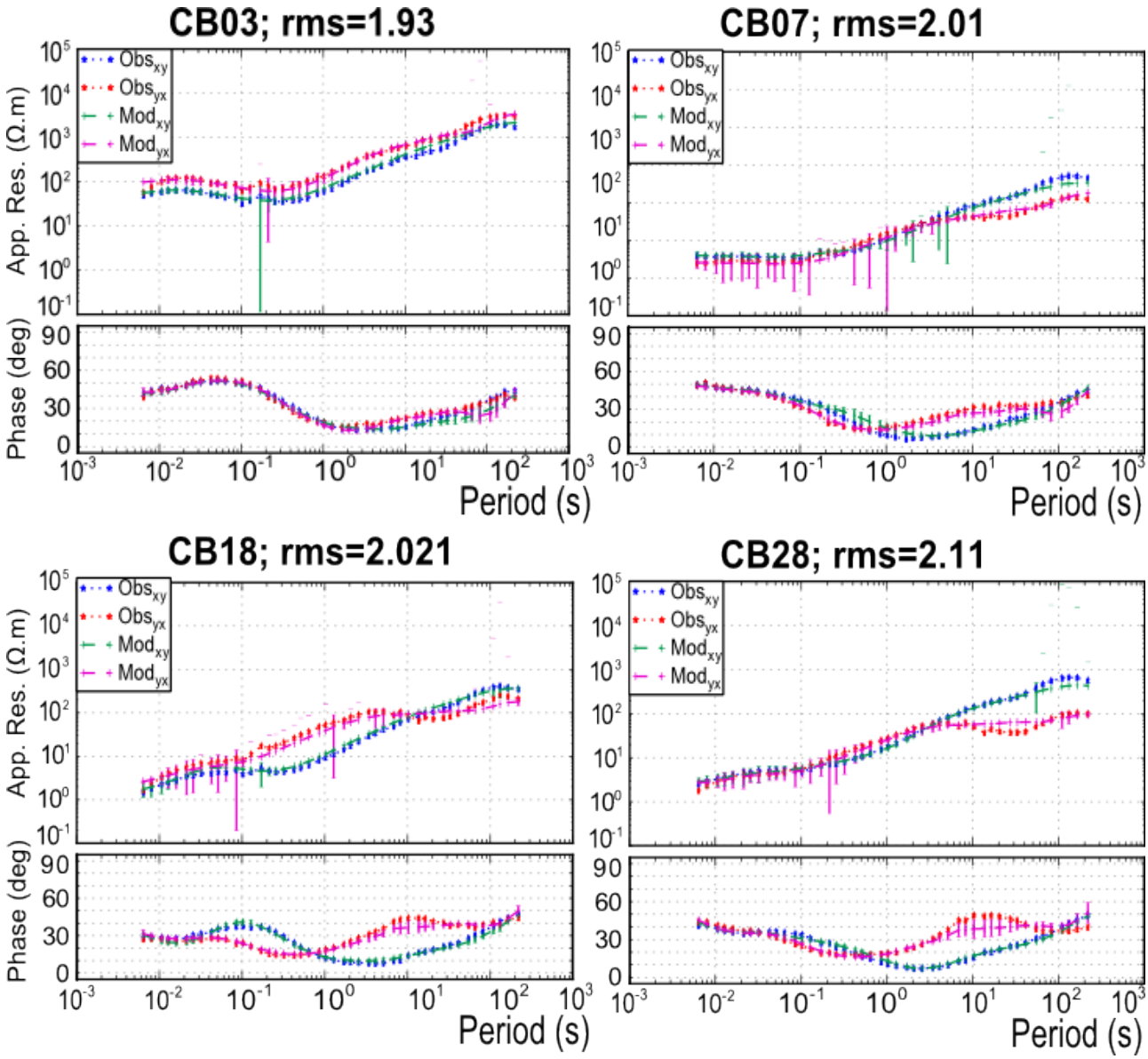

Figure 6 Sample data curves of TE and TM mode data plotted with the inversion response for stations CB03, CB07, CB18 and CB28. The blue line represents the line of best fit for the best TE mode (Obs_{xy}), red line for the TM mode (Obs_{yx}); and for the OCCAM modelled data, the green line is the TE mode (Mod_{xy}), and pink is the TM mode (Mod_{xy}). The RMS misfit is listed beside the station name. Overall data fit is good, with the modelled responses following very similar trends and values to the observed data, except at very long periods where the modelled TM mode shows more variation to the observed TM mode.

INVERSION PROCESS

The Cariewerloo MT data set was inverted and modelled using the OCCAM2D algorithm of deGroot-Hedlin and Constable (1993) which uses an over parameterised model scheme seeking the smoothest possible model at a given level of misfit. It uses the finite element forward code for 2D MT modelling of Wannamaker (1987) .

Sensitivity Analysis

To determine the robustness of the inversion models, different sets of conditions were tested until ideal inversion parameters were established. Parameters changed were the modes of inversion and resistivities of the homogenous half spaces. Separate inversions of the TE and TM modes were run in addition to a TE-TM mode. The TE mode highlighted more conductive layers, while the TM mode highlighted more resistive layers and observed more heterogeneity at depth. Bimodal inversion included important features of both. Simultaneous inversion of differing homogenous half spaces of, 1, 10, 100, 1000 and 10 000 Ωm showed very little variation of resistivity structure between inversions.

Unconstrained MT Model

Figure 7 shows the unconstrained, non static shift corrected inversion model using OCCAM2D. The starting model was a homogeneous half space of 100 Ωm with respective apparent resistivity and phase error floors of 10% and 5%, producing a model with an RMS misfit value of 2.74 and roughness value of 575. A revised error floor was applied to the apparent resistivity in the TE mode, increasing from 10% to 50% to

allow for undetermined along-strike static affects. The resulting model had a lower RMS misfit of 2.26 and a similar roughness of 594 indicating a better data fit.

AEM Forward Model constrained MT Model

The AEM technique uses a very high sampling frequency of 75 kHz that is sampled at a much closer spacing than the MT, resolving conductivity structures in great detail. This high-resolution data can be incorporated into the regularisation grid of the MT model as a-priori information. In OCCAM this was achieved by introducing a prejudice file containing the corresponding AEM resistivity values into the inversion process. The tau value determines the weighting of the Prejudice File on the inversion mode with a value of 1 using only resistivity values from the Prejudice file.

Seven different inversions were run with the same model parameters of the unconstrained MT model, but with the addition of a prejudice file. The tau value varied from 1, 0.7 and 0.5. The prejudice file compared the outputs of two different depths, 500 m representing the full resistivity profile and 200 m representing the average depth of confidence in the resistivity values. The resulting MT model always observed a highly conductive layer at the base of the prejudice file. This could be inferred as a discrepancy between the MT and AEM models perhaps caused by static shift offset, or that the AEM better defines a conductive body at this depth. All models have a similar RMS misfit and roughness values, indicating mathematically they were very similar. Using a-priori geological knowledge we determined the most geological plausible model was an inversion with a prejudice file to a depth of 500 m with a tau weighting of 1 with a resulting RMS value of 2.5 and roughness factor of 167.

Static Shift Corrected Model

Static shift is a complex process which is caused by the build up of electric charges on shallow inhomogeneities that MT cannot resolve (Pellerin & Hohmann 1990, Macnae et al. 1998). The estimation and removal of static shift may be necessary as it can significantly affect the resistivities and depths resolved by models (Sternberg et al. 1988, Tournerie et al. 2007). Simpson and Bahr (2005) suggest three broad static shift correction schemes; (1) averaging (statistical) techniques, (2) long-period corrections which rely upon deep structure homogeneity and (3) short-period corrections which rely upon near-surface measurements. The latter two schemes have been tested here.

SHORT PERIOD

EM techniques such as TEM and AEM are not affected by electric field distortions as they use magnetic fields for subsurface characterisation so can establish shallow surface resistivities with more confidence than MT (Sternberg et al. 1988, Pellerin & Hohmann 1990, Meju 1996).

Resistivity values were manually entered into a predefined mesh with cell sizes that correspond to the AEM inversion cell sizes. These AEM resistivity values were forward modelled over the bandwidth 10^4-10^2 Hz. The resulting AEM apparent resistivity and phase curves are in the frequency domain and can be plotted directly with the MT curves. The subsequent vertical offset between the AEM curve and the two MT modes, TE and TM, can be directly compared and manually scaled as seen in Figure 10.

In Figure 11, the correction factor for each mode (TE and TM) at each MT station is shown. Four stations were affected by a resistive surface inhomogeneity causing higher apparent resistivity curves, 13 stations were affected by a conductive surface causing a lower apparent resistivity curve, eight stations showed a split TE and TM mode and four stations were unaffected by static shift. There was no correlation showing that either the TE or the TM mode was more susceptible to static shift. The resulting model had an RMS misfit of 2.08 and a roughness value of 445.

LONG PERIOD

The second correction scheme assumes the deep structure is observed by all stations in the survey and therefore the long-period magnetic transfer functions are similar. This allows a shift factor to be determined based on this deeper information. Curves were corrected at periods with coincident phases as suggested by Berdichevsky et al. (1998). This investigation used the apparent resistivity value of ~130 Ωm at a period of 101 sec, manually shifting curves to this nominated value. The resulting MT model had an RMS misfit of 2.19 and roughness value of 356.

COMPARISON OF STATIC SHIFT CORRECTIONS

Short period and long period static shift corrected MT data were inverted using the same parameters as the unconstrained model but with respective static shift corrected EDI files. The two static shift corrected models show very similar conductivity structures with only two notable differences that both underlie stations CB19 – CB22. The AEM short period corrected model displays higher resistivity at depths of 400 m and lower resistivity at 20 km. The RMS misfit was slightly lower for the short-period

AEM based static corrected inversion of the MT, indicating a better fit. As a result the AEM constrained static shift model will be used in comparison with other inversions in the rest of this paper.

OBSERVATION AND RESULTS

The three MT models; unconstrained MT resistivity model Figure 7; AEM constrained MT resistivity model Figure 8 and static shift corrected Figure 11, demonstrate the same general conductivity trends in the top 700 m; a conductive surface layer ~50 m thick, resistive intermediate layer of varying thickness 30 – 500 m and second thicker conductivity layer which all overlies a significantly resistive basement. A general conductivity interpretation structure is seen in Figure 7.

Upper crust

At the surface there is a thin linear highly conductive (0.1 – 10 Ωm) layer labelled Cs1 in Figure 7. Cs1 has an average thickness of ~30 m thickening towards the south to ~100 m. Additionally, the AEM model shows more detail within this layer, delineating two very thin (~15 m) conductive bodies.

The resistivite layer, R1, is discontinuous across the MT profile and can be divided into two regions, R1 and R2. The resistive structure R1 underlies the southern stations of CB29 to CB12 and varies in thickness and resistivity between the models. The unconstrained resistivity model and to a greater extent the static shift corrected resistivity model show a relatively linear discontinuous body of varying resistivity ~30 Ωm. In the AEM constrained resistivity model, the resistive body is a more resistive

(100-1000 Ωm) linear body that extends the entire transect length, thinning towards the north.

The second resistive body ~40 Ωm, nominated R2, is present at the northern end of the MT transect. The unconstrained and static shift corrected models and to a greater extent the AEM constrained models show a 200 m thick body that rapidly thins towards the south before disappearing.

The bottom conductive layer, Cu1, varies greatly with structure and depth between the three models. The unconstrained MT model shows a conductive (~10 Ωm) body of 200 m in the south, Cu1, and a much thicker (~500m) more conductive (1-5 Ωm) body dipping 15˚ towards North, Cu2. The static shift corrected model shows a similar pattern with a thinner Cu1 layer of higher conductivity (>1 Ωm). The AEM constrained model shows differing structures with a consistent thin linear layer of high conductivity (>0.1 Ωm) at a depth of 500m which is thicker under the North of the transect.

Two vertical regions of homogenous conductivity ~ 70 Ωm are observed under stations CB10-CB13 and CB20-CB22 and are particularly highlighted in the static shift corrected model. Vertical displacement of the conductivity layers indicate offset between conductivity layers. This is consistent with previous analysis of the pseudosection which suggested two faults in these regions.

Deeper structures

The aforementioned highly conductive upper crust overlies a resistive basement consistent with previous deep MT soundings in the Gawler Craton (Heinson et al. 2006, Maier et al. 2007, Thiel & Heinson 2010). Within the resistive basement, there are three structures of interest; a significantly resistive anomaly in the south Rx, framed by a conductive anomaly Cf, and a conductive anomaly in the north Cx. The resistive body Rx to the south extends over a distance of 20 km from a depth of 2.5 – 23 km with resistivity in excess of 10 000 Ωm. The more conductive region Cf connects with the inferred faults in the shallow region.

Anomalies of enhanced conductivity in the north (~200 Ωm) are highlighted as Cf, in the north underlying stations CB04, CB03 and CB02. The unconstrained model shows a 45˚ dipping pattern. The static shift corrected and AEM constrained models differ showing vertical conductivity under CB01 with a very high conductivity point (>1 Ωm) between stations CB04 and CB03. This conductivity point was initially thought to be an inversion artefact, however further inversions were run which retained the 45˚ structure.

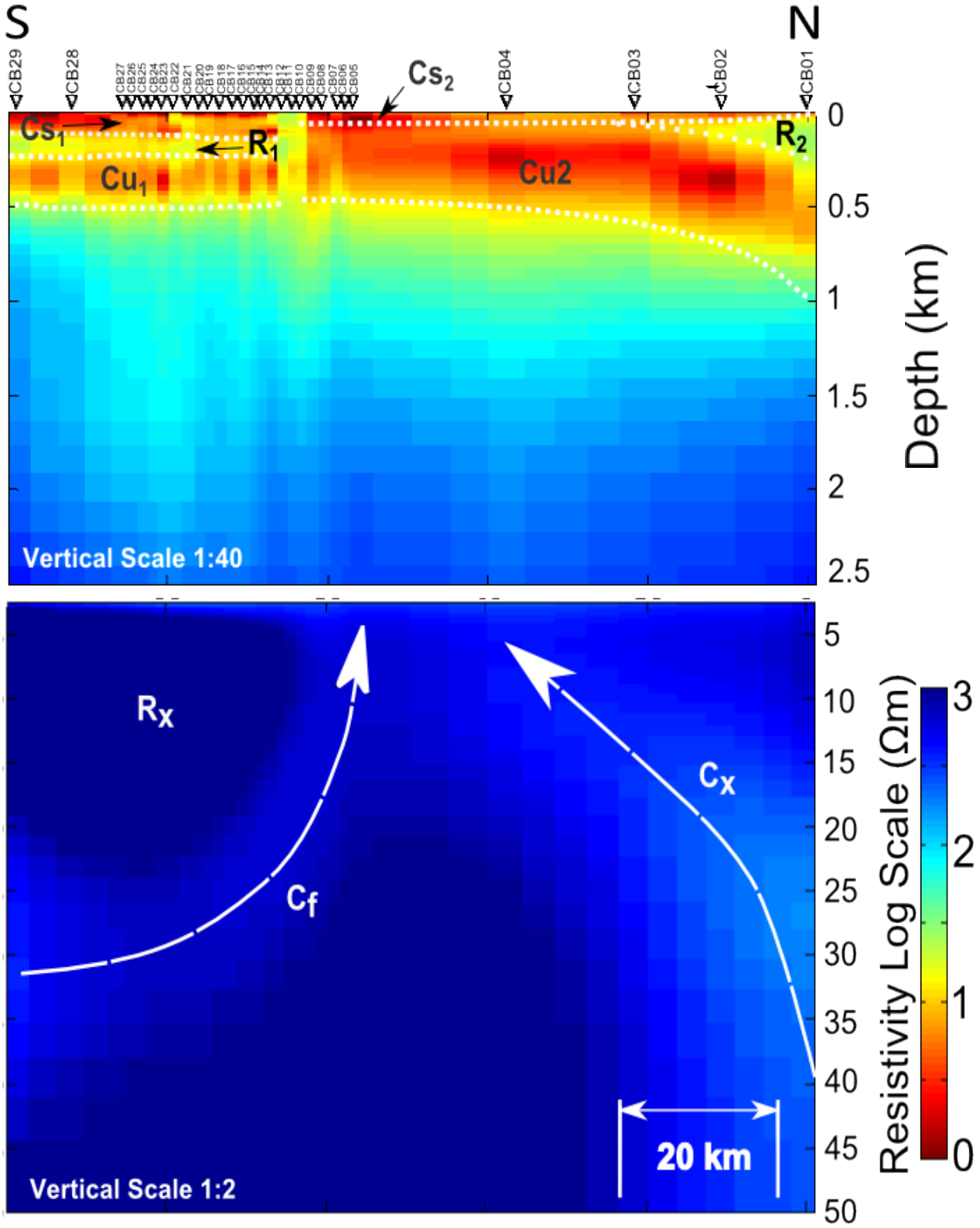

Figure 7 The unconstrained MT model, a 2D inversion model using OCCAM, with apparent resistivity and phase errors floor of 10% and 5% respectively for the TM mode and 50% and 5% for TE mode. The top figure has a vertical exaggeration of 40 and shows a conductive surface layer, Cs_1, resistive layers R_1 and R_2 and conductive layers Cu_1 and Cu2 overlying a significantly resistive basement. The bottom figure has a vertical exaggeration of 2 showing a significantly resistive anomaly, Rx which is bordered by a conductive fluid, Cf. Another conductive region Cx underlies the stations in the north.

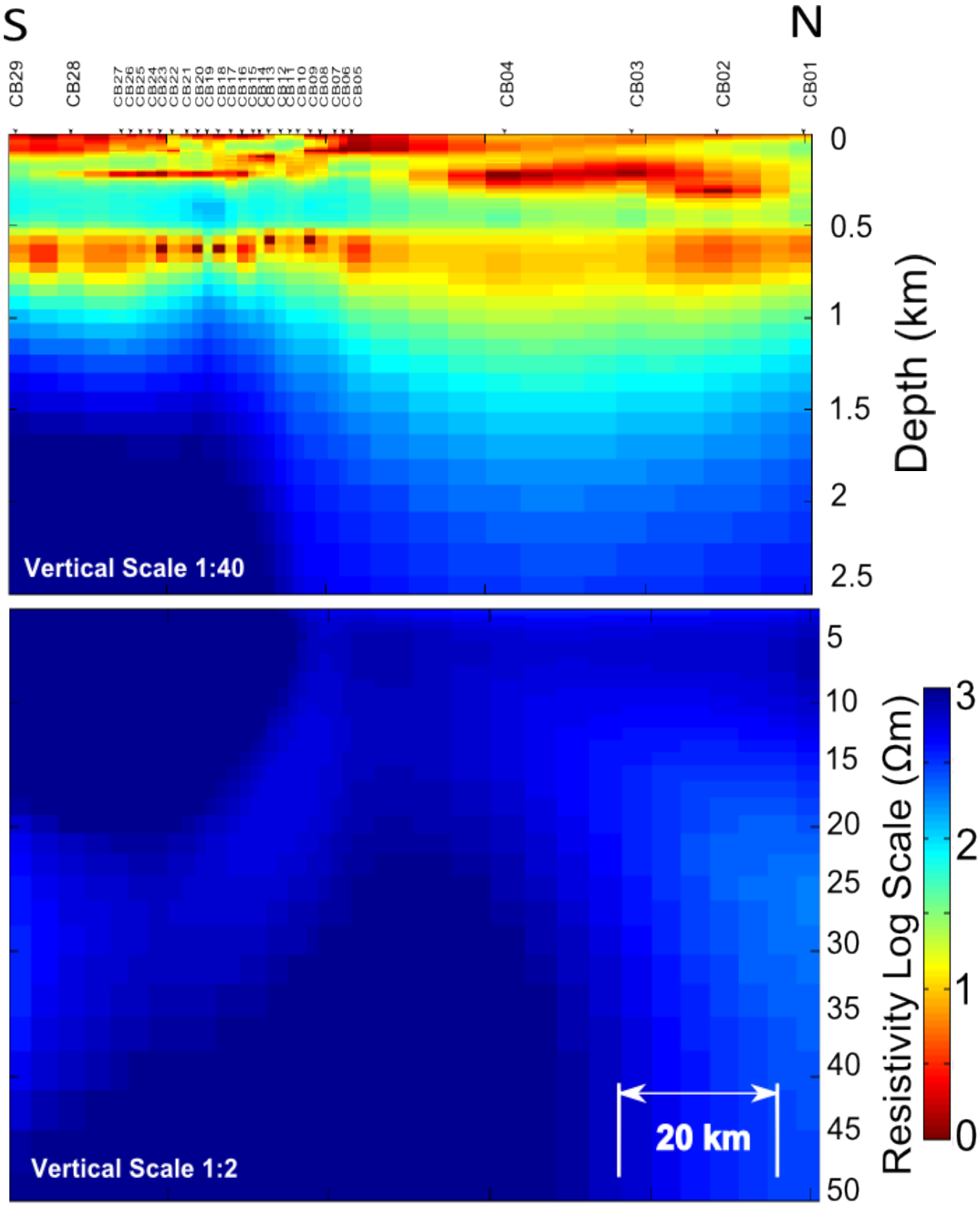

Figure 8 The AEM constrained MT model, a 2D OCCAM (MT) model using the AEM resistivity values as a-priori information with a tau value of 1 to a depth of 500 m with respective apparent resistivity and phase error floors of 10% and 5% for TM mode and 50% and 5% for TE mode. RMS misfit value of 2.5 and roughness value of 169.

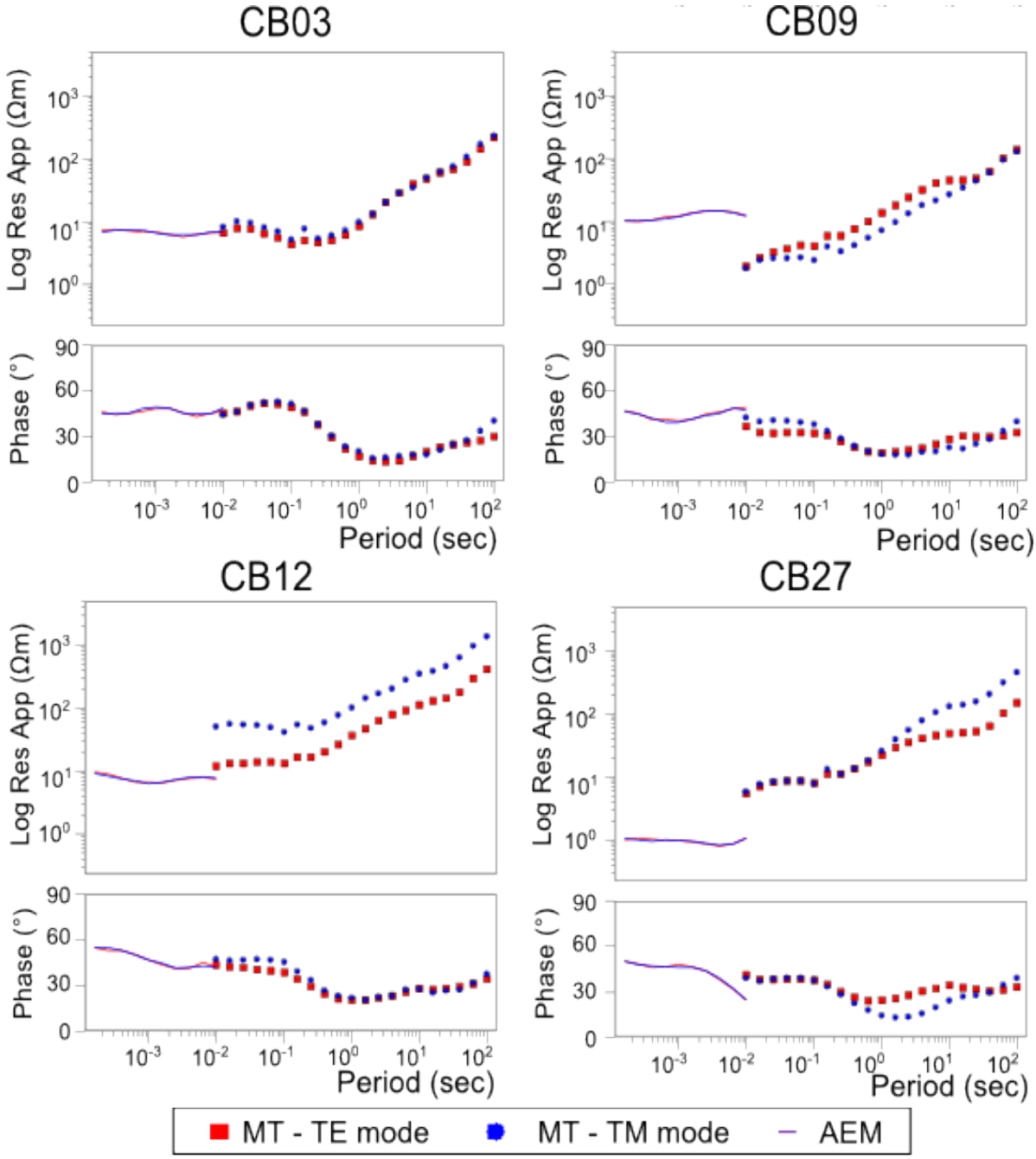

Figure 9 Apparent Resistivity and Phase sounding curves for AEM (blue line) and two MT modes, TE (red square) and TM mode (blue dot). Four stations are shown; CB03 shows vertical offset of the apparent resistivity, not requiring static shift corrections, CB09 shows MT apparent resistivity curves lower than the AEM requiring an upwards shift (typical of resistive surface areas); CB12 shows a split TE and TM mode.

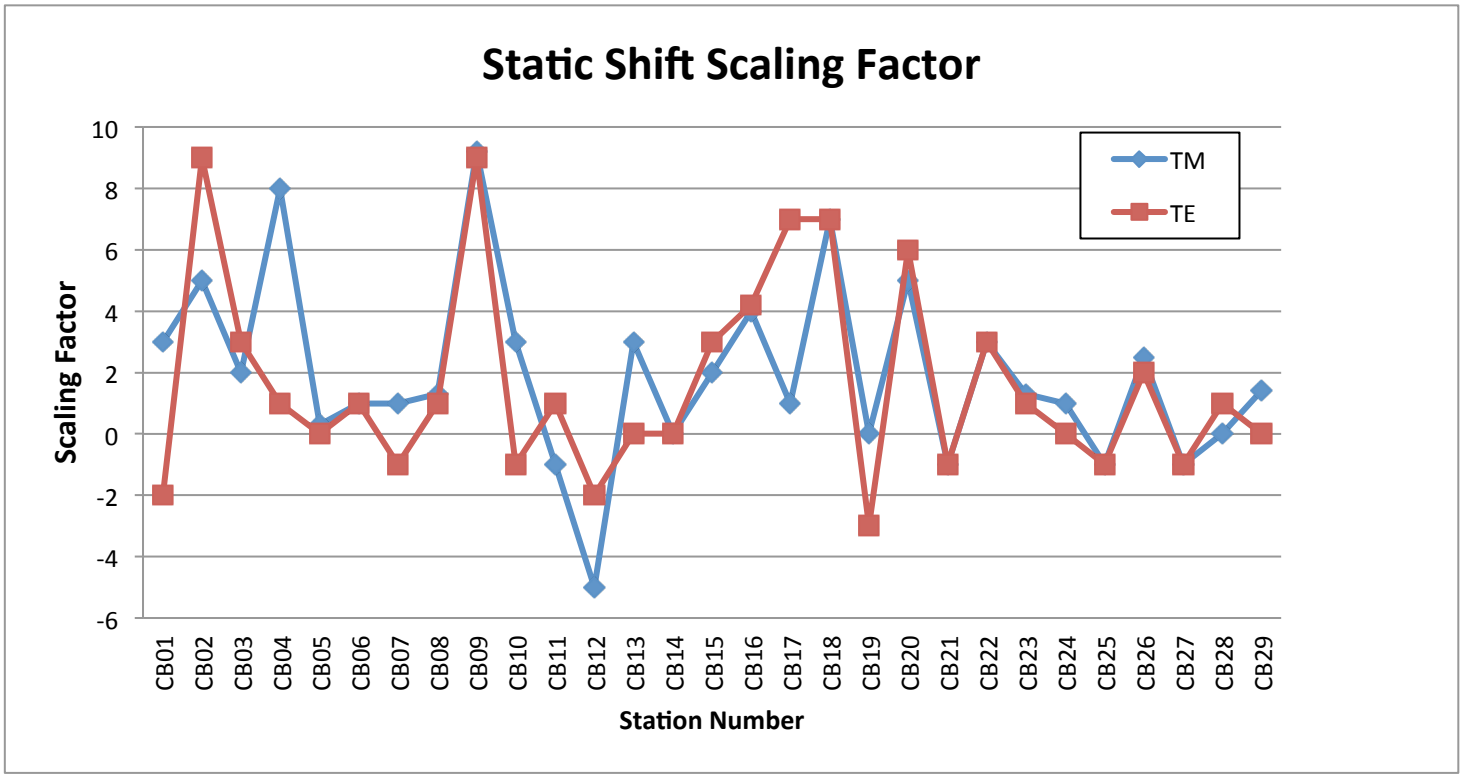

Figure 10 A graph plotting the scaling factor the apparent resistivity in the TE mode (blue) and TM mode (red) were scaled by (y-axis) against the site number (x-axis). Positive scaling factors indicate an upward shift, increasing the apparent resistivity, typical on conductive surface layers. Negative scaling factors indicate a downward shift decreasing the apparent resistivity that is typical of resistive surface layers. There is no clear correlation with one mode being more susceptible to static shift.

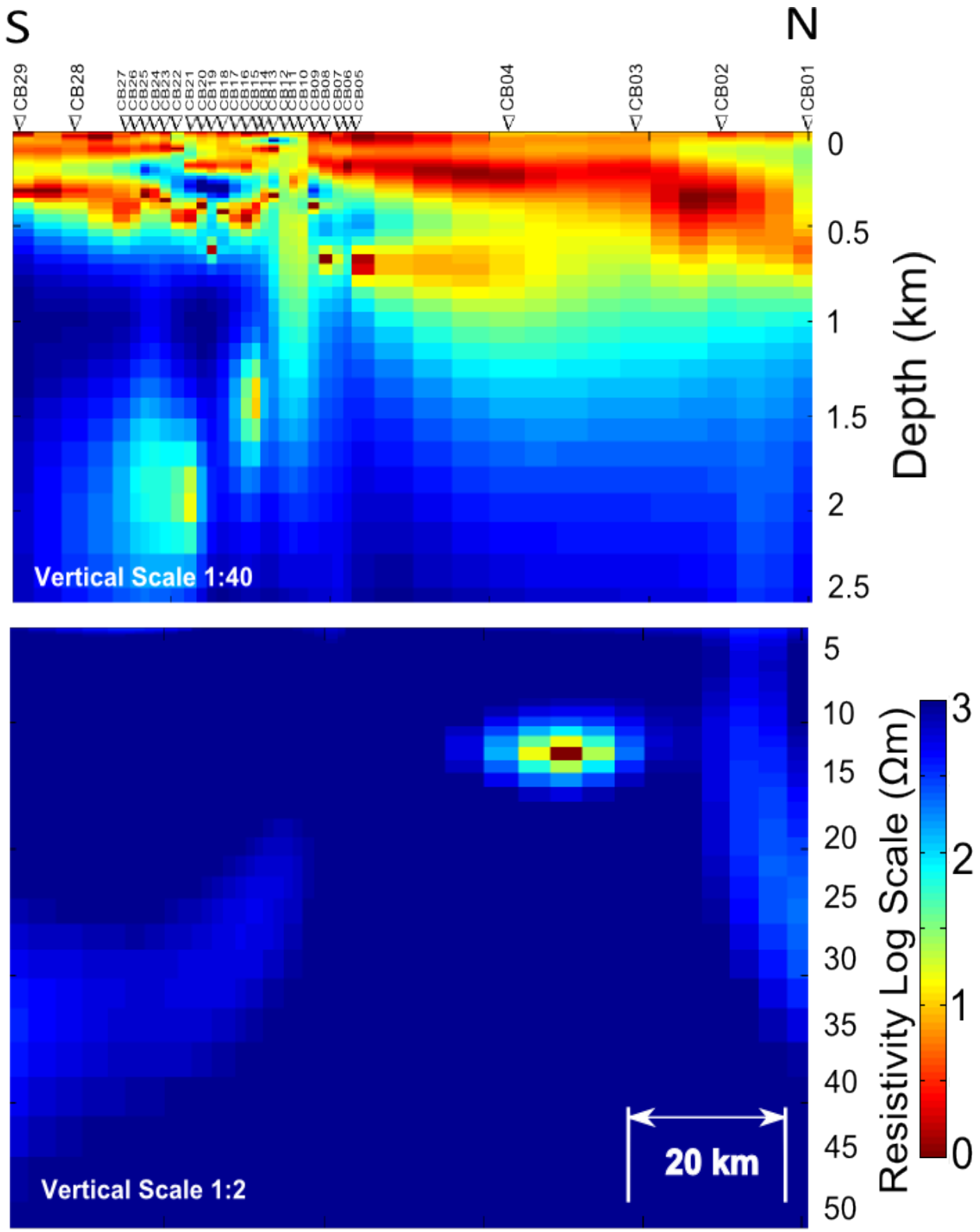

Figure 11 The AEM static shift corrected MT model, a 2D inversion model using OCCAM2D with respective apparent resistivity and phase error floors of 10% and 5% for TM mode and 50% and 5% for TE mode. RMS misfit value of 2.08and roughness value of 445.

DISCUSSION

Model Comparison

The three resistivity models produced; unconstrained, AEM constrained and static shift corrected, all obtained RMS misfit values of ~2.5 suggesting mathematically there is not much difference between the resistivity models. These three MT resistivity models show very similar levels of complexity, imaging highly conductive surficial layers overlying resistive basement. Since EM exploration for unconformity-related deposits identifies regions of anomalous conductivity against a resistive background, it is important to resolve resistive structures. AEM constrained and static shift corrected models better define resistive layers allowing greater contrast between resistivities. These two models also introduce much more heterogeneity into the model, better defining fault offsets and confining regions of conductivity to thin layers. At deeper structures, the AEM constrained resistivity model observes continuity of conductive phases framing resistive structures, where as the static shift corrected resistivity model shows discrete bodies between stations. The AEM constrained model is better suited for exploration of unconformity-related uranium; hence a combined method of MT using AEM as a-priori information is better than either the MT or AEM method alone.

Geological Interpretation

A geological interpretation of the MT model is shown in Figure 12, constrained by shallow drill holes in the area. The highly conductive (~1 Ωm) layer Qs is interpreted to be a combination of Quaternary and Adelaidean sediments with a strong presence of salt and the Adelaidean sequences. The MT models do not have the resolution to distinguish between the two. The intermediate resistive layer that sits immediately below this, is the Pandurra Formation, (Pf) which increases in thickness as it gently dips towards the north. The bottom conductive layer sits between the resistive Pandurra Formation and resistive basement and is thought to be an alteration zone associated with the unconformity at the base of the Pandurra. The three models observe varying thicknesses of the resistive rock packages which is most likely a function of the highly conductive surface sediments having a shielding effect on deeper structures.

Structures in the deeper crust suggests the presence of highly resistive (<10 000Ωm) crustal blocks with crustal scale boundaries being highlighted by more conductive regions. These regions have conductivities one to two orders of magnitude smaller and are most likely palaeo-flow pathways along boundaries of the resistive crustal blocks. Alternatively this area could include very small amounts of graphite (Orange 1989, Bedrosian 2007) or pore fluids (Hyndman & Hyndman 1968, Wei et al. 2001, Li et al. 2003) which cause higher conductivity.

Potential Targets

The MT imaged the unconformity surface as well as two faults which are potential fluid pathways. High conductivity was observed at these regions; however there was not

enough detail in the resolution of the MT model. This is due to the survey having a cell size in the order of 40 m looking for a resistive halo which will be within 25 m of the unconformity surface. The unconformity surface was a thick (~200 m) conductive layer. Thus these small scale conductive alteration halos could not be detected and it cannot be established whether ingress or egress systems are present in the region. In the MT study of Tuncer et al. (2006) station spacing was 300 m, compared to 1000 m used in this survey, allowing much finer spatial resolution of the AEM. However this survey did highlight prospective transport and trap sites where faults intersect the unconformity. Further MT surveys of smaller station spacing would establish whether unconformity-related mineralisation is present.

CONCLUSIONS

This study has shown that MT is an effective tool for mapping depth to basement in regions of conductive cover. The highly conductive unconformity imaged with MT in this study is relatively linear, dipping towards the north in the north of the transect. Detailed resolution of the unconformity surface was not achieved as the stations were too widely spaced, not allowing zones of silicification and alteration halos to be observed. However, two fault structures can be seen offsetting the resistivity layers. Additionally, MT has provided new information about deeper crustal heterogeneity highlighting highly resistive blocks which have been accreted with less resistive zones bordering these resistive blocks indicative of fossil fluid pathways.

The application of AEM a-priori structure and static correction resulted in two additional resistivity models of the crust. The AEM constrained model enhanced the

resolution of the surficial structure but created an anomalous conductive region at the base of this structure which could not be determined to be either real or not. The static shift corrected model introduced more heterogeneity into the model but was considered more geologically plausible from prior geological knowledge.

ACKNOWLEDGEMENTS

The author would like to express their gratitude to the honours and PhD students at the University of Adelaide for their support and assistance in discussions about the ins and outs of the MT method, especially Sebastian Schnaidt and Kate Robertson, Tania Wilson of Geological Survey of South Australia for sharing her geological knowledge; Goran Boren for his attention to detail with instrumentation; Jared Peacock for his fast MT station deploying skills, help with handling Python and Spyder and his OCCAM2D processing code, Dr Stephan Thiel for his support and my supervisors, Tania Dhu of the Geological Survey of South Australia for access to resources and support and Professor Graham Heinson for his patience, assistance and for introducing me to MT.

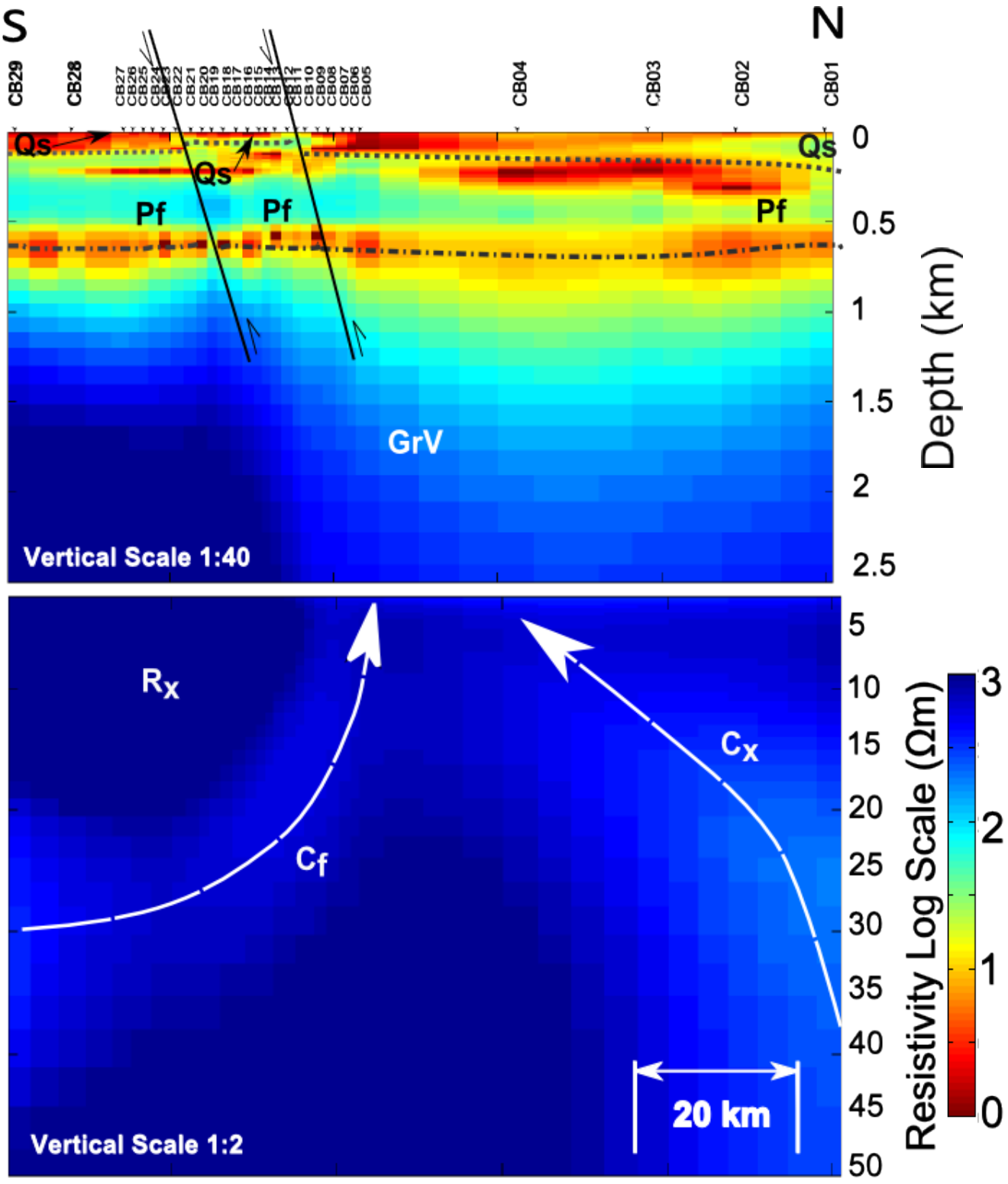

Figure 12 A geological interpretation overlain onto the AEM constrained MT model which uses the AEM as a-priori information. The shallow interpretation consists of conductive layer, Qs, which are the Quaternary sediments and Adelaidean Sequences which contain high amounts of salt. Pf is the Pandurra formation which is resistive sandstone, GrV are the resistive Gawler Range Volcanics and also includes deeper crystalline basement. Rx is an anomalous resistive body and Cf and Cx are regions of lower resistivity thought to be palaeo fluid paths. Two thrust faults are observed, F1 and F2, which offset layers Cs1 and Pf. The unconformity surface is highlighted by the dashed line.

REFERENCES

ALEXANDRE P., KYSER K., THOMAS D., POLITO P. & MARLAT J. 2009. Geochronology of unconformity-related uranium deposits in the Athabasca Basin, Saskatchewan, Canada and their integration in the evolution of the basin. *Mineralium Deposita* **44**, 41-59.

BEDROSIAN P. A. 2007. MT+, integrating magnetotellurics to determine Earth structure, physical state, and processes. *Surveys in geophysics* **28**, 121-167.

BELPERIO A. & FREEMAN H. 2004. Common geological characteristics of Prominent Hill and Olympic Dam-Implications for iron oxide coppergold exploration models. *Australian Institute of Mining Bulletin, Nov-Dec. Issue*, 67-75.

BERDICHEVSKY M. N., DMITRIEV V. I. & POZDNJAKOVA E. E. 1998. On two-dimensional interpretation of magnetotelluric soundings. *Geophysical Journal International* **133**, 585-606.

BERDICHEVSKY M. N. & LOGUNOVICH R. F. 2008. Electromagnetic excitation of asthenospheric conducting zones. *Izvestiya Physics of the Solid Earth* **44**, 527-536.

CAGNIARD L. 1953. Basic theory of the magneto-telluric method of geophysical prospecting. *Geophysics* **18**, 605-635.

CAMECO CORPORATION 2010. *Uranium operations*.

CHAVE A. D. & JONES A. G. 2012. *The Magnetotelluric Method: Theory and Practice*.

CHAVE A. D. & THOMSON D. J. 2004. Bounded influence magnetotelluric response function estimation. *Geophysical Journal International* **157**, 988-1006.

COWLEY W. M. 1991. The Pandurra Formation. *Geological Survey; Department of Mines and Energy South Australia*.

COWLEY W. M. 1993. Pandurra Formation. *The geology of South Australia* **1**, 139-142.

DE VESLUD C. L. C., CUNEY M., LORILLEUX G., ROYER J. J. & JÉBRAK M. 2009. 3D modeling of uranium-bearing solution-collapse breccias in Proterozoic sandstones (Athabasca Basin, Canada)--Metallogenic interpretations. *Computers & Geosciences* **35**, 92-107.

DEGROOT-HEDLIN C. & CONSTABLE S. 1993. Occam's inversion and the North American Central Plains electrical anomaly. *Journal of geomagnetism and geoelectricity* **45**, 985-999.

DEROME D., CATHELINEAU M., LHOMME T. & CURLEY M. 2003. Fluid inclusion evidence of the differential migration of H< sub> 2</sub> and O< sub> 2</sub> in the McArthur River unconformity-type uranium deposit (Saskatchewan, Canada). Possible role on post-ore modifications of the host rocks. *Journal of Geochemical Exploration* **78**, 525-530.

DHU T., GOUTHAS G., REED G., WILSON T., COWLEY W. & FAIRCLOUGH M. 2010a. Geophysical mapping of an unconformity in 3D, Cariewerloo Basin, South Australia. *AIG GeoComputing Abstracts*.

DHU T., REED G., WILSON T., COWLEY W., HEATH P., GOUTHAS G. & M. F. 2010b. Unconformity-related uranium in SA geophysical analysis of the Cariewerloo Basin. *ASEG Extended Abstracts* **2010**, 1-4.

EGBERT G. D. 2002. Processing and interpretation of electromagnetic induction array data. *Surveys in geophysics* **23**, 207-249.

FAIRCLOUGH M. C. 2006. Uranium: South Australia state of play. *MESA Journal* **41**, 8-11.

FANNING C. M., FLINT R. B. & PREISS W. V. 1983. Geochronology of the Pandurra Formation. *Geological Survey of South Australia Quarterly Geological Notes* **88**, 11-16.

FAYEK M. & KYSER T. K. 1997. Characterization of multiple fluid-flow events and rare-earth-element mobility associated with formation of unconformity-type uranium deposits in the Athabasca Basin, Saskatchewan. *The Canadian Mineralogist* **35**, 627-658.

HAND M., REID A. & JAGODZINSKI L. 2007. Tectonic framework and evolution of the Gawler craton, southern Australia. *Economic Geology* **102**, 1377-1395.

HECHT L. & CUNEY M. 2000. Hydrothermal alteration of monazite in the Precambrian crystalline basement of the Athabasca Basin (Saskatchewan, Canada): implications for the formation of unconformity-related uranium deposits. *Mineralium Deposita* **35**, 791-795.

HEINSON G. S., DIREEN N. G. & GILL R. M. 2006. Magnetotelluric evidence for a deep-crustal mineralizing system beneath the Olympic Dam iron oxide copper-gold deposit, southern Australia. *Geology* **34**, 573-576.

HYNDMAN R. & HYNDMAN D. 1968. Water saturation and high electrical conductivity in the lower continental crust. *Earth and Planetary Science Letters* **4**, 427-432.

JEFFERSON C. W., THOMAS D. J., GANDHI S. S., RAMAEKERS P., DELANEY G., BRISBIN D., CUTTS C., PORTELLA P. & OLSON R. A. 2007. Unconformity-associated uranium deposits of the Athabasca Basin, Saskatchewan and Alberta. *Bulletin - Geological Survey of Canada* **588**, 23.

JONES A. G. 1988. Static shift of magnetotelluric data and its removal in a sedimentary basin environment. *Geophysics* **53**, 967-978.

KEELING J. L., MAUGER A. J., WILSON T. & RAVEN M. D. 2011. Diagenetic clay mineral distribution in Mesoproterozoic sandstones of the Cariewerloo Basin, South Australia–implications for uranium mobilisation.

LAMBERT I., JAIRETH S., MCKAY A. & MIEZITIS Y. 2005. Why Australia has so much uranium. *AusGeo News* **80**.

LI S., UNSWORTH M. J., BOOKER J. R., WEI W., TAN H. & JONES A. G. 2003. Partial melt or aqueous fluid in the mid-crust of Southern Tibet? Constraints from INDEPTH magnetotelluric data. *Geophysical Journal International* **153**, 289-304.

MACNAE J., LAY L. & WESTON L. 1998. Measurement of static shift in MT and CSAMT surveys. *Exploration Geophysics* **29**, 494-498.

MAIER R., HEINSON G., THIEL S., SELWAY K., GILL R. & SCROGGS M. 2007. A 3D lithospheric electrical resistivity model of the Gawler Craton, Southern Australia. *Applied Earth Science* **116**, 13-21.

MASON M. G., THOMSON B. P. & TONKIN D. G. 1978. Regional stratigraphy of the Beda Volcanics, Backy Point Beds and Pandurra Formation on the southern Stuart Shelf, South Australia. *South Australian Geological Survey Quarterly Geological Notes* **66**, 2-9.

MEJU M. A. 1996. Joint inversion of TEM and distorted MT soundings: Some effective practical considerations. *Geophysics* **61**, 56-65.

ORANGE A. S. 1989. Magnetotelluric exploration for hydrocarbons. *Proceedings of the IEEE* **77**, 287-317.

PELLERIN L. & HOHMANN G. W. 1990. Transient electromagnetic inversion: A remedy for magnetotelluric static shifts. *Geophysics* **55**, 1242-1250.

SIMPSON F. & BAHR K. 2005. *Practical magnetotellurics*. Cambridge Univ Pr.

SKIRROW R. G. 2009. *Uranium mineral systems: Processes, exploration criteria and a new deposit framework*. Geoscience Australia.

STERNBERG B. K., WASHBURNE J. C. & ANDERSON R. G. 1985. Investigation of MT static shift correction methods. *1985 SEG Annual Meeting*.

STERNBERG B. K., WASHBURNE J. C. & PELLERIN L. 1988. Correction for the static shift in magnetotellurics using transient electromagnetic soundings. *Geophysics* **53**, 1459-1468.

THIEL S. & HEINSON G. 2010. Crustal imaging of a mobile belt using magnetotellurics: an example of the Fowler Domain in South Australia. *Journal of Geophysical Research* **115**, B06102.

TIKHONOV A. N. 1950. On determining electrical characteristics of the deep layers of the earth's crust. **2**, 295-297.

TONKIN D. G. 1980. *Report on deep stratigraphic drillhole EC 21.* Australia D. o. M. a. E. S.

TOURNERIE B., CHOUTEAU M. & MARCOTTE D. 2007. Magnetotelluric static shift: Estimation and removal using the cokriging method. *Geophysics* **72**, F25-F34.

TUNCER V. 2007. Exploration for unconformity type uranium deposits with audio-magnetotelluric data: A case study from the McArthur River Mine, Saskatchewan, Canada. Master of Science in Geophysics thesis, Faculty of Graduate Studies and Research, Univeristy of Alberta, Edmonton, Alberta (unpubl.).

TUNCER V., UNSWORTH M. J., SIRIPUNVARAPORN W. & CRAVEN J. A. 2006. Exploration for unconformity-type uranium deposits with audiomagnetotelluric data: a case study from the McArthur River mine, Saskatchewan, Canada. *Geophysics* **71**, B201-B209.

VILJANEN A., NEVANLINNA H., PAJUNPÄÄ K. & PULKKINEN A. 2001. Time derivative of the horizontal geomagnetic field as an activity indicator, pp. 1107-1118.

WANNAMAKER P. E., STODT, J.A., & RIJO, L. 1987. A stable finite element solution for two-dimensional magnetotelluric modelling. *Geophysical Journal of the Royal Astronomical Society* **88**, 277-296.

WEI W., UNSWORTH M., JONES A., BOOKER J., TAN H., NELSON D., CHEN L., LI S., SOLON K. & BEDROSIAN P. 2001. Detection of widespread fluids in the Tibetan crust by magnetotelluric studies. *Science* **292**, 716-719.

WILSON M. & KYSER T. 1987. Stable isotope geochemistry of alteration associated with the Key Lake uranium deposit, Canada. *Economic Geology* **82**, 1540-1557.

WILSON T., BOSMAN S., HEATH P., GOUTHAS G., COWLEY W., MAUGER A., BAKER A., GORDON G., DHU T. & FAIRCLOUGH M. 2010a. The potential for unconformity-related uranium mineralisation in the Pandurra Formation, South Australia: an international multidisciplinary collaboration. PayDirt Uranium Conference(unpubl.).

WILSON T., BOSMAN S., HEATH P., GOUTHAS G., COWLEY W., MAUGER A., BAKER A., GORDON G., DHU T. & FAIRCLOUGH M. 2010b. The search for unconformity-related uranium mineralisation in the Pandurra Formation, South Australia: an international multidisciplinary collaboration. *MESA Journal* **58**, 9-15.

WORLD NUCLEAR ASSOCIATION 2010. *Geology of uranium deposits, January 2010*.

APPENDIX

Appendix A: MT Site locations and processing parameters for the Cariewerloo Basin, South Australia

	MGA Zone 53						1000 Hz Processing				100 Hz			
Site Name	**Eastings (m)**	**Northings (m)**	**Elevation (m)**	**Declination**	**Latitude**	**Longitude**	Day	Remote Reference Start Time	Remote Reference End Time	Remote Reference Station	Day	Remote Reference Start Time	Remote Reference End Time	Remote Reference Station
CB01	694840	6574314	119	6.921	-30.9486	137.0396	151	070000	090000	CB01	151	030000	223000	CB16
CB02	694724	6563479	122	6.936	-31.0463	137.0405	151	070000	090000	CB02	151	030000	225000	CB16
CB03	693170	6552808	169	6.945	-31.1428	137.0263	150	070000	090000	CB03	150	040000	210000	CB01
CB04	693622	6536745	124	6.969	-31.2875	137.0341	151	070000	090000	CB04	151	030000	240000	CB16
CB05	693813	6517395	88		-31.6255	137.0434	153	070000	090000	CB05	153	020000	220000	CB20
CB06	693825	6516395	97		-31.471	137.0402	153	070000	090000	CB06	153	020000	220000	CB06
CB07	694926	6515262	118		-31.481	137.052	153	070000	090000	CB07	153	020000	220000	CB20
CB08	693045	6513606	89	6.999	-31.4963	137.0325	154	070000	090000	CB08	154	010000	224000	CB20
CB09	692683	6512348	114		-31.5077	137.029	154	070000	090000	CB09	154	020000	224000	CB20
CB10	692557	6510865	108		-31.5211	137.0279	154	070000	090000	CB10	155	030000	220000	CB26
CB11	693032	6509765	104		-31.5309	137.0332	154	070000	090000	CB11	154	032000	224000	CB20
CB12	693459	6508521	106	7.007	-31.542	137.0379	157	070000	090000	CB12	156	023000	230000	CB26
CB13	693975	6507029	118		-31.5554	137.0436	156	070000	090000	CB13	156	023000	230000	CB26
CB14	692306	6505977	109		-31.5652	137.0262	156	070000	090000	CB14	156	030000	220000	CB26
CB15	693775	6505009	113		-31.5737	137.0419	156	070000	090000	CB15	156	050000	230000	CB26
CB16	693721	6503627	114	7.015	-31.5861	137.0416	151	070000	090000	CB16	151	000000	223000	CB01
CB17	693740	6502293	116		-31.5982	137.0421	151	070000	090000	CB17	151	010000	223000	CB01
CB18	693767	6500665	105		-31.6128	137.0427	151	070000	090000	CB18	151	020000	223000	CB01
CB19	693815	6499265	104		-31.6254	137.0435	151	070000	090000	CB19	151	050000	220000	CB01
CB20	693829	6498047	73	7.023	-31.6364	137.0438	154	070000	090000	CB20	154	050000	150000	CB10
CB21	693859	6496715	95		-31.6484	137.0444	154	070000	090000	CB21	154	030000	220000	CB10
CB22	693877	6494834	100		-31.6654	137.045	154	070000	090000	CB22	154	030000	220000	CB10
CB23	691874	6493548	85		-31.6773	137.0241	154	070000	090000	CB23	154	030000	220000	CB10
CB24	692997	6492191	90	7.028	-31.6894	137.0362	155	070000	090000	CB24	155	012000	233000	CB10

CB25	694079	6490928	97		-31.7006	137.0479	155	070000	090000	CB25	155	030000	220000	CB10
CB26	694194	6489581	95		-31.7127	137.0494	155	070000	090000	CB26	155	030000	220000	CB10
CB27	694411	6488438	89		-31.723	137.0519	155	070000	090000	CB27	155	040000	220000	CB10
CB28	691504	6482290	90	7.043	-31.7789	137.0224	157	070000	090000	CB28	157	030000	220000	CB15
CB29	691173	6475411	100	7.045	-31.841	137.0203	157	070000	090000	CB29	157	030000	220000	CB15